



The effect of annealing atmosphere on the structural properties of FeSiBPCu alloys with different silicon content

Katarína Sedlačková¹ · Beata Butvinová² · Milan Pavúk¹ · Július Dekan¹ · Stanislav Sojak¹ · Patrik Novák¹ · Jozef Sitek¹

Accepted: 27 October 2022 / Published online: 8 November 2022
© The Author(s), under exclusive licence to Springer Nature Switzerland AG 2022

Abstract

NANOMET-type soft magnetic alloys of $\text{Fe}_{82}\text{Si}_4\text{B}_{10}\text{P}_3\text{Cu}_1$ and $\text{Fe}_{78}\text{Si}_8\text{B}_{10}\text{P}_3\text{Cu}_1$ were studied. Nanocrystalline alloys were prepared by annealing the amorphous precursors at a temperature of 420 °C for 20 and 60 min in vacuum and in Ar atmosphere. The effect of the annealing atmosphere and time of annealing on the alloy structural and magnetic properties were investigated by X-ray diffraction (XRD), Mössbauer spectroscopy (MS), magnetic measurements and atomic force microscopy (AFM). XRD unveiled partial crystallization of the $\text{Fe}_{82}\text{Si}_4\text{B}_{10}\text{P}_3\text{Cu}_1$ alloy and confirmed amorphous structure of the $\text{Fe}_{78}\text{Si}_8\text{B}_{10}\text{P}_3\text{Cu}_1$ alloy. The technique also indicated larger grain size after annealing in vacuum as compared to that in argon. MS disclosed the effect of the silicon content on the annealed alloys microstructure, namely the lower relative volumetric fraction of the A8 crystalline phase component for the alloy with 8 at. % Si as compared to the alloy with 4 at. % Si. Variations of the parameters reflecting the magnetic microstructure were also observed and are discussed with relation to different annealing times and atmospheres. Magnetic measurements showed better soft magnetic properties for sample with 8 at. % Si whose coercivity was lower as well as the determined magnetization work. They also indicated lower coercivity for argon annealed samples and showed that longer annealing times are reflected in the increased resultant coercivity. For both studied compositions, the AFM measurements inspecting the morphology of the sample surfaces manifested the presence of lower protrusions on the surfaces of the vacuum annealed samples as compared to the argon annealed ones, where also larger agglomerates were disclosed.

Keywords NANOMET · FeSiBPCu · Nanocrystalline · Amorphous · Mössbauer spectroscopy · AFM

This article is part of the Topical Collection on Proceedings of the International Symposium on the Industrial Applications of the Mössbauer Effect (ISIAME2022), Olomouc, Czech Republic Edited by Libor Machala

✉ Katarína Sedlačková
katarina.sedlackova@stuba.sk

¹ Institute of Nuclear and Physical Engineering, Slovak University of Technology in Bratislava, Ilkovičova 3, 812 19 Bratislava, Slovakia

² Institute of Physics, Slovak Academy of Sciences, Dúbravská Cesta 9, 845 11 Bratislava, Slovakia

1 Introduction

Nanocrystalline Fe-based alloys prepared from their amorphous precursors by controlled crystallization process during thermal annealing yield unique soft magnetic properties, like low core loss, high permeability, low magnetostriction, sufficiently high saturation magnetic flux density and low coercivity, which are attractive for many industrial applications. Since the last decades, numerous chemical compositional combinations have been studied and compared to tailor the magnetic microstructure of both amorphous alloys and their nanocrystalline counterparts. Variety of alloying elements, such as Si, B, Cu, Nb, Zr, P, Ni, Co and many others are nowadays subject of investigations with the aim to explore their effect on the structural parameters like the grain size, their composition and spatial distribution [1]. As a result, the foreseen soft magnetic properties defined by high saturation magnetization, B_S , and low coercivity, H_C , can be achieved by optimisation of both the composition and the crystallization conditions.

The microstructure and crystallization kinetics of the most prominent FINEMET (FeSi-based), NANOPERM (FeZr-based) and HITPERM (FeCo-based)-type alloys have been widely investigated because of their superior (high temperature) soft magnetic properties [2]. Although the metal elements such as Nb, Zr, Mo, etc. comprised in these alloys are effective in reducing the diffusion rate of Fe during annealing and hence limit the growth of the crystalline grains, they result in major decrease of B_S and not least also an increase the alloy cost [3]. More recently, the soft magnetic Fe-Si-B-P-Cu alloy system known as the NANOMET was developed [4]. NANOMET alloys exhibit high saturation magnetization close to 2 T, low H_C of 7–10 A/m, small magnetostriction of $2\text{--}3 \times 10^{-6}$ and ultra-low losses ($W_{1.7/50} \sim 0.4$ W/kg). This excellent magnetic softness predestines NANOMET alloys for applications in motors and transformers for electrical appliances, where a remarkable improvement in energy consumption due to outstanding low core losses was reported [5]. Another positive economical aspect of NANOMET-type alloys is their lower cost, as they do not require expensive rare-metals, such as niobium in FINEMETs.

As the glass-forming ability of the high Fe-content Fe-Si-B-P-Cu alloys is relatively low, the structure of the melt-spun alloys is sensitive to the impurities of raw materials and melt-spinning process and the prepared ribbons may contain primary α -Fe nuclei in the amorphous matrix [6]. The annealing of precursors with pre-existing α -Fe grains may influence the structural evolution of the prepared nanocrystalline alloys.

In this work, we have inspected the NANOMET-type structure of Fe-Si-B-P-Cu with different Si content, namely the two compositions of $\text{Fe}_{82}\text{Si}_4\text{B}_{10}\text{P}_3\text{Cu}_1$ and $\text{Fe}_{78}\text{Si}_8\text{B}_{10}\text{P}_3\text{Cu}_1$, were studied. In general, in Fe-Si-B-P-Cu alloys, silicon (Si) and boron (B) are the elements increasing the glass forming ability, addition of Cu refines the primary particles and promotes the uniformity of grain dispersion and the role of phosphorous (P) is to refine the grain structure of the alloys. During annealing process, B is rejected from the α -Fe grains and accumulated in the amorphous rest, and Si is excluded from the amorphous matrix and partitioned in the α -Fe particles [1]. The differences in the Si content in the same system usually result in various content of the crystalline phase (e.g., Si superseding Fe in Fe-Si-B-Cu alloys decreases the volume fraction of the crystalline phase [7]) and in various structure and composition of nanograins. The formation of nanograins with high Si content during primary crystallization is responsible for the increase of permeability and decrease of magnetostriction (defined as the change of dimensions of ferromagnetic material during the process of magnetisation [1]). Si addition can also enhance the thermal stability of the nanocrystalline material.

Besides the above-mentioned chemical composition and melt-spinning process, the thermal annealing conditions are considerably affecting the alloy microstructure and resulting soft magnetic properties as well. Optimisation of the gas atmosphere, heating rate, temperature and duration of the annealing procedure can facilitate the formation of a fine and uniform nanostructure and magnetic softening of the resultant nanocrystalline alloys. In case of FINEMETs (FeCuNbSiB), the effect of annealing ambience was found to be especially pronounced for Si-poor compositions, where the materials respond to annealing-induced macroscopic heterogeneity with magnetoelastic anisotropy [8, 9].

Therefore, besides studying the effect of different Si content, we have also explored how the annealing conditions (annealing ambience and heating duration) influence the structure and magnetic properties of the resultantly prepared nanocrystalline samples. With this aim, alloys of both studied compositions were subjected to thermal annealing in different atmospheres (vacuum and argon) for 20 and 60 min. Mössbauer spectroscopy and X-ray diffraction techniques were used to analyse the bulk structural properties, which we mutually compared with the resultant magnetic properties obtained by hysteresis loop measurements. Due to foreseen macroscopic heterogeneity and surface effects playing a crucial role for the studied alloys macroscopic characteristics [10], we have also employed a surface sensitive technique of atomic force microscopy to explore the morphology of alloy surfaces.

2 Materials and methods

Amorphous ribbons of 6.5 mm width and $18.5 \div 22.5$ μm thickness, were produced from master alloys of two compositions, i.e., $\text{Fe}_{82}\text{Si}_4\text{B}_{10}\text{P}_3\text{Cu}_1$ (samples labelled Si-4) and $\text{Fe}_{78}\text{Si}_8\text{B}_{10}\text{P}_3\text{Cu}_1$ (samples labelled Si-8), by a planar-flow casting method on a single-roller copper wheel with a surface cooling rate of about 10^6 K/s on air at the Slovak Academy of Sciences in Bratislava. Samples of about 10 cm length were annealed in vacuum (pressure between 5×10^{-2} and 9×10^{-4} Pa) and in flowing technical argon (furnace was not evacuated before annealing) at 420 °C with duration of 20 and 60 min. Temperature rise time is not included into the annealing duration time. The annealing temperature was chosen with respect to the crystallization onset temperatures T_{x1} determined from the first crystallization peaks of the differential scanning calorimetry (DSC) curves, which are 400 °C and 420 °C for Si-4 and Si-8 samples, respectively [9]. Obviously, Fe-Si-B-P-Cu alloys require lower annealing temperatures as compared with conventional FINEMETs due to the lack of the grain-growth blocker, as Nb or Mo. Longer annealing times (10ths of minutes) were chosen considering to be more practical for industrial production process.

XRD analysis was carried out using a Bruker D8 ADVANCE diffractometer equipped with an X-ray tube with cobalt anode operating at 12 kW. Diffraction patterns were recorded in Bragg–Brentano geometry in a wide scan range, from 20° to 110° with a step size of 0.025° and a time per step of 2 s. Analysis of diffraction patterns was performed using DIFFRAC.EVA software and TOPAS. The crystallinity was computed from the diffraction pattern as the percentage of the reduced area corresponding to the crystalline phase. To calculate the crystallite size, the Lorentzian convolution was applied using TOPAS software. The uncertainty in their determination is about 10%. The structure of sample surfaces was inspected by X-ray diffraction measurements performed in grazing incidence geometry (GIXRD). Grazing incidence measurement was carried out with copper $K\alpha$ radiation and the angle of incidence was 1°. All scans were measured in a range from 20° to 110°.

The Mössbauer spectra were measured at room temperature using a Wissel Mössbauer spectrometer with the $\text{Co}^{57}(\text{Rh})$ source in transmission geometry. Spectrometer was calibrated using a standard foil of $\alpha\text{-Fe}$ at room temperature. The spectra were evaluated by CONFIT program [11] allowing simultaneous treatment of crystalline components and residual amorphous phases using individual lines and distributions of hyperfine magnetic fields. The hyperfine parameters of the spectra including relative component area (A), internal hyperfine magnetic field (B_{hf}) as well as the ratio of the second (and fifth) to the third (and fourth) line intensities of a sextet in Mössbauer spectrum (A_{23}) were derived in the evaluation procedure. The accuracy in their determination is about 2% for the relative area, about 0.5 T for the hyperfine magnetic field and about 0.1 for the A_{23} parameter.

In magnetic measurements, the hysteresis loops were recorded using a digitizing hysteresis graph at standard ac (frequency 21 Hz) sinusoidal field H excitation in Helmholtz drive coils in longitudinal direction on 10 cm long strips. The loops recorded for strips are corrected for demagnetization by plotting the polarization J against the internal field H_i computed as $H_i = H_{\text{ext}} - DJ/\mu_0$, where the demagnetization factor D was evaluated from the strip dimensions using elliptic integral calculation. Each sample had its own demagnetization factor calculated as the sample dimensions varied slightly from one to other. The values of D were $(5 \pm 0.5) \times 10^{-5}$. Apart from the uncertainty caused by not attaining actual magnetic saturation, the accuracy of the magnetic polarization J_s calculation is $\pm 3.5\%$.

Atomic Force Microscopy measurements were performed on a Veeco Dimension Edge™ microscope. A Bruker TESP-V2 silicon probe with a nominal tip radius of 7 nm was used to scan the ribbon surfaces. The cantilever spring constant is 37 N/m. Scanning was performed in tapping mode. The quality of the probe tip and the correct setting of the microscope were verified by measuring the surface of the calibration grating. The microscope is placed on a pneumatic vibration-isolation table and covered with a soundproof cover during the measurement. The cover also prevents airflow, which could interfere with the measurement. The shiny side of the ribbons was examined because it is flatter. It is the side that was not in physical contact with the rotating cooling wheel during production. Instead, it was only exposed to air. The height of the protrusions will be analysed as this parameter is not affected by the sharpness of the tip.

3 Results and discussion

3.1 X-ray diffraction

Crystallographic structure of the studied samples was inspected by X-ray diffraction technique (XRD). Diffractograms of the as-cast samples and samples after thermal annealing in both annealing ambiances are shown in Fig. 1. Diffractogram of the Si-8 as-cast sample (Fig. 1b, green line) shows only a broad peak which confirms its amorphous structure. In the case of Si-4 sample (Fig. 1a), however, besides the broad halo attributed to a disordered structure, also sharp peaks are present. They correspond to an $\alpha\text{-Fe}$ crystalline phase occurring frequently in the as cast ribbons of high Fe content, as mentioned before. According to the diffraction pattern analysis procedure described above, its abundance in the Si-4 sample was determined to be as high as $(30 \pm 10)\%$.

XRD analysis of the annealed samples confirmed their two-phase composition. Besides amorphous rest, the crystalline bcc-Fe(Si) phase corresponding to the first stage of crystallization occurring close to 400 °C was identified. The corresponding

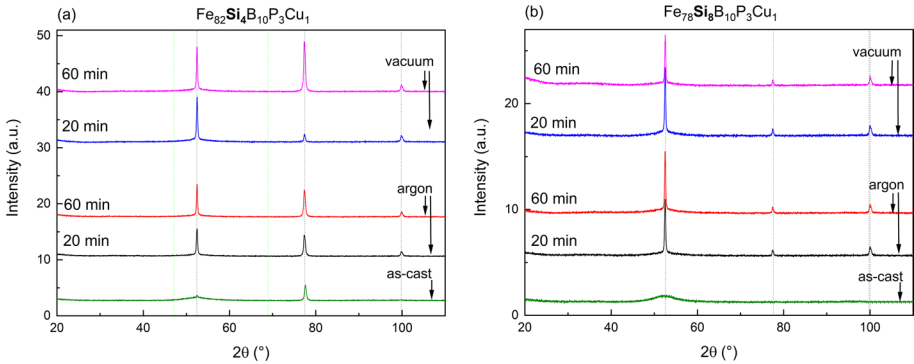


Fig. 1 XRD patterns acquired from the as-cast $\text{Fe}_{82}\text{Si}_4\text{B}_{10}\text{P}_3\text{Cu}_1$ (a) and $\text{Fe}_{78}\text{Si}_8\text{B}_{10}\text{P}_3\text{Cu}_1$ (b) alloys

Table 1 Crystal size and abundance of the crystalline phase determined from XRD measurements for $\text{Fe}_{82(78)}\text{Si}_{4(8)}\text{B}_{10}\text{P}_3\text{Cu}_1$ alloys annealed for 20 and 60 min at 420 °C in vacuum and argon (uncertainty ~ 10%)

Alloy		Grain size [nm]		Crystallinity [%]	
		420 °C/ 20 min	420 °C/ 60 min	420 °C/ 20 min	420 °C/ 60 min
$\text{Fe}_{82}\text{Si}_4\text{B}_{10}\text{P}_3\text{Cu}_1$	vacuum	58	59	31	52
	Ar	53	56	44	45
$\text{Fe}_{78}\text{Si}_8\text{B}_{10}\text{P}_3\text{Cu}_1$	vacuum	74	81	35	36
	Ar	68	80	34	34

diffraction pattern exhibit a lattice parameter of about 2.86 Å for all annealed samples. The size of the crystals along with the abundance of the respective crystalline phase is listed in Table 1 for all studied samples. If comparing Si-4 and Si-8 sample, we can notice lower grain size of Si-4 (53 ÷ 59 nm) as compared to Si-8 samples (68 ÷ 81 nm). The size of the nanocrystals tends to increase with longer annealing times for both compositions and both annealing atmospheres. The crystalline phase abundance in Si-4 alloy is about 31% after 20 min-vacuum annealing. After 20 min in argon it reaches, however, about 44%. Even though the uncertainty in the crystallinity determination is as high as 10%, the observed tendency might suggest promoted crystallization by argon atmosphere in the 4% Si-alloy. For the Si-8 samples, the content of crystalline phase after 20 min is similar for both ambiances (35% for vacuum and 34% for argon). Longer annealing time of 60 min seems to affect more markedly only Si-4 alloy annealed in vacuum (increase from 31 to 52%).

The samples surfaces were inspected by XRD in grazing incident geometry. Grazing incidence measurement provides information from a depth of about 0.15 μm and was realized to test the phase composition of the surface layers (e.g., presence of oxides). Though, no oxides and no other phases and as compared to the bulk material were identified.

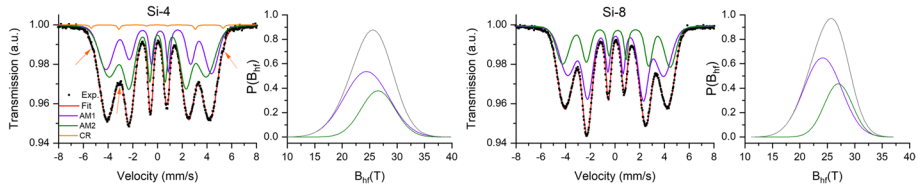


Fig. 2 Mössbauer spectra of the as-cast $\text{Fe}_{82}\text{Si}_4\text{B}_{10}\text{P}_3\text{Cu}_1$ (left) and $\text{Fe}_{78}\text{Si}_8\text{B}_{10}\text{P}_3\text{Cu}_1$ (right) alloys

Table 2 Parameters of Mössbauer spectra of the as-cast $\text{Fe}_{82(78)}\text{Si}_{4(8)}\text{B}_{10}\text{P}_3\text{Cu}_1$ alloys (A —relative area of the component, B_{hf} —average magnetic induction of hyperfine magnetic fields, DW —distribution width, A_{23} —ratio of the second (and fifth) to the third (and fourth) line intensities)

Alloy	Component	Mössbauer parameters			
		A_{rel} [%]	B_{hf} [T]	DW [T]	A_{23} [-]
$\text{Fe}_{82}\text{Si}_4\text{B}_{10}\text{P}_3\text{Cu}_1$	AM1	60.0	24.4	9.8	2.26
	AM2	38.9	26.5	7.4	1.52
	average		25.4		1.99
$\text{Fe}_{78}\text{Si}_8\text{B}_{10}\text{P}_3\text{Cu}_1$	AM1	64.2	24.2	8.74	2.95
	AM2	35.8	27.0	6.5	1.97
	average		25.2		2.60

3.2 Mössbauer spectroscopy

Mössbauer spectroscopy (MS) was used to inspect the changes in the short-range order and the resultant magnetic microstructure of the $\text{Fe}_{82}\text{Si}_4\text{B}_{10}\text{P}_3\text{Cu}_1$ (Si-4) and $\text{Fe}_{78}\text{Si}_8\text{B}_{10}\text{P}_3\text{Cu}_1$ (Si-8) as-cast and nanocrystalline alloys. Especially the hyperfine magnetic fields, the relative abundancies corresponding to the various iron sites and the direction of the net magnetic moments were followed with respect to different annealing conditions. It has to be emphasized that due to the transmission geometry mode of the Mössbauer technique, the information on the bulk material is obtained from the measurements.

3.2.1 As-cast alloys

Mössbauer spectra of the as-cast samples show a broad asymmetrical sextet demonstrating amorphous nature of the melt-spun alloys (Fig. 2). On the envelope of the spectrum corresponding to the sample with 4% of Si (left side of Fig. 2) one can recognize a first sign of the crystallization indicated by arrows. It is manifested as presence of a sharp sextet with hyperfine parameters consistent with bcc-Fe phase. Its relative fraction with respect to the amorphous rest is, however, very low and laid on the border of detection ($\sim 1.2\%$). Hence, the XRD technique proved to be much more sensitive to recognise the crystallization begin in the as-cast alloys as compared to MS.

The fitting of the broad spectral part corresponding to the amorphous rest was performed using two Gaussian-shaped hyperfine distributions, $P(B_{hf})$ (shown at right, next to the spectrum) representing structurally and magnetically different environments of the Fe resonant atoms. The hyperfine parameters arising from the fitting procedure are presented in Table 2, where B_{hf} is a parameter describing the average hyperfine spin-exchange interaction between magnetic atoms in the sample, DW is a distribution width, A_{23} is a

parameter reflecting the mean orientation of the local magnetization and A_{rel} is the relative area of the component corresponding to the volumetric fraction of the respective phase.

The shape of the Mössbauer spectra of the as-cast samples shown in Fig. 2 obviously points at some structural changes due to different silicon content. Although the resultant average hyperfine field, B_{hf} , is practically the same for both compositions, the observed spectra differences manifested quantitatively in the process of spectra analysis especially as a redistribution of the applied components. In Table 2 one can notice the changes of the relative areas, A_{rel} , corresponding to the lower-field and higher-field distributions (designated $AM1$ and $AM2$) as well as the corresponding B_{hf} and DW values. Differences in these parameters are also manifested in the distributions $P(B_{hf})$ depicted in Fig. 2.

Another hyperfine parameter of the Mössbauer spectra which is very sensitive to changes in the magnetic microstructure is the A_{23} parameter reflecting the mean orientation of the local magnetization. It reaches its minimum value when the spins and the vector of net magnetization are perpendicular to the ribbon plane and the maximum value of A_{23} parameter is consistent with net magnetic moment lying within the ribbon plane. The average values of A_{23} of the as-cast alloys listed in Table 2 indicate, that increased silicon content results in slight turn of the mean local magnetization to the ribbon plane.

3.2.2 Annealed alloys

Crystalline phases formed in Fe-Si alloys with Si content under about 10 at. % during controlled annealing prefer to form disordered structure with three different type of sites corresponding to Fe central atoms of the body centred cubic lattice having 8, 7 and 6 nearest-neighbour iron atoms and the residual sites occupied by Si atoms (marked as A8, A7 and A6 configuration, respectively) [12]. The internal magnetic field values corresponding to a particular site are not dependent on the percentage of Si atoms present in the alloy but only on the nearest neighbours, namely it decreases by about 0.08 H_{Fe} for each Si neighbour. The Si content influences only the probabilities for an Fe atom to have 8, 7 or 6 nearest neighbour iron atoms (i.e., A8, A7 or A6 configuration). With higher Si content (> 10 at. % of Si), Fe_3Si structure with bcc lattice is formed [13].

Accordingly, our fitting model comprised several components describing specific site occupancy in the studied nanocrystalline alloys, i.e., broadened hyperfine field distributions (Gaussian-shaped) and single magnetic splittings. While the sharply defined hyperfine fields (single sextets) can be attributed to the Fe atoms always surrounded by a given number of nearest neighbours, a distribution of magnetic splitting can be expected for Fe atoms in the sites surrounded by a random distribution of Fe and Si atoms. To describe the A-site configurations in disordered alloy systems, the approaches using distributions of B_{hf} [12] as well as single sextets [7], can be applied. Due to disordered structure, no strict distinction between distributions and single sextets is made in our fitting model, rather than the components were attributed to different structural iron sites according to the respective hyperfine field values. Due to high Fe content of the studied alloys, the A8, A7 and A6 configurations have the highest probability of being occupied by Fe atoms as compared to other coordination numbers (not considered in the fitting procedure). B_{hf} values attributable to the observed configurations are about 33 T, 31.5 T and 28.5 T for A8, A7 and A6 coordination surroundings, respectively. B_{hf} values lying in-between these values or below might result from combined surroundings structure and/or partly ordered interfacial region manifested in the spectra often as a narrower distribution of hyperfine fields or as a broader sextet.

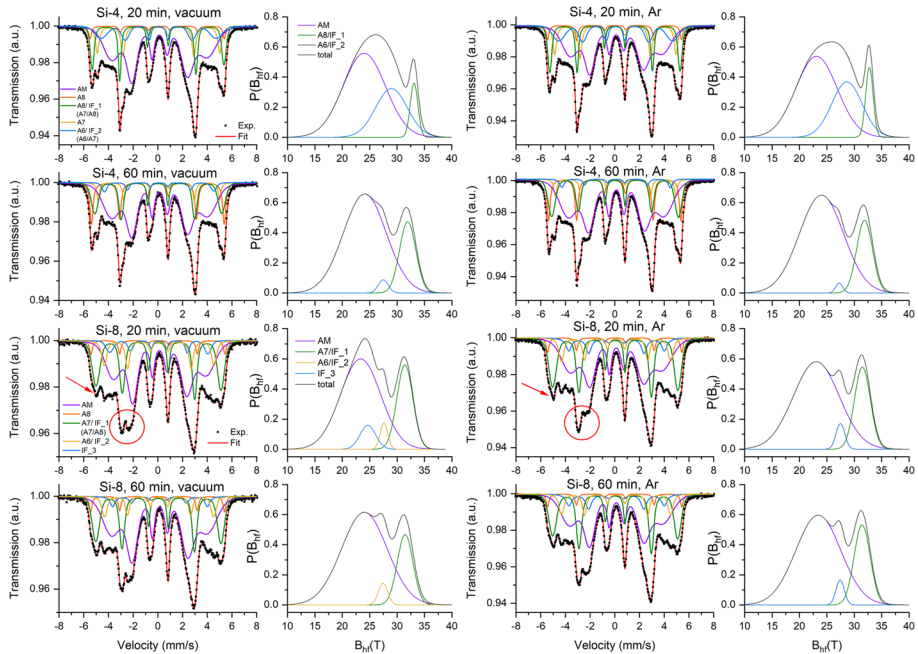


Fig. 3 Mössbauer spectra of the $\text{Fe}_{82}\text{Si}_4\text{B}_{10}\text{P}_3\text{Cu}_1$ (first two rows) and $\text{Fe}_{78}\text{Si}_8\text{B}_{10}\text{P}_3\text{Cu}_1$ (last two rows) alloys annealed in vacuum (left column) and argon (right column)

Mössbauer spectra of the Si-4 and Si-8 samples annealed in vacuum and argon for 20 and 60 min along with the corresponding distributions of the hyperfine fields are shown in Fig. 3. As compared to the as-cast samples, the spectra collected after thermal annealing reflect different stage of sample crystallization. First, we can notice that Mössbauer spectra of the samples with lower silicon content (Si-4) (the first two rows of the spectra in Fig. 3) depict sharply featured shape suggesting higher crystallinity as compared to the samples with the higher silicon content (Si-8) (the last two rows of the spectra in Fig. 3). Comparing Si-4 samples annealed for 20 and 60 min, one can notice a pronounced increase of the A8 crystalline component by about 10% for both annealing atmospheres (the orange-coloured lines in the spectra) and a slight rise of the overall crystalline phase comprising A8 and A7 components (the ochre-coloured lines) from about 17 to 22% for the vacuum annealing, and from 19 to 21% for the argon annealing. As mentioned before, no strict distinction between crystalline and amorphous phase is foreseen to be derived from the spectra due to its complexity, rather than existence of some interfacial region is proposed to be considered (represented by the green and the blue-coloured lines). The hyperfine field values of the green components (labelled A8/IF_1) are close to that of A8 structure for 20 min annealed samples; though for longer annealing times, the average B_{hf} shifted below 32 T. The blue component (labelled A6/IF_2) of 20 min annealed alloys shows B_{hf} values close to 29 T, which is consistent with A6 structure; for 60 min annealing times it is suppressed and the corresponding B_{hf} decreased for both annealing atmospheres. Low-hyperfine field component of the spectra can be unambiguously assigned to disordered (amorphous) rest (the violet-coloured line in the spectra) and its relative fraction varied from 47 to 55%. The mean hyperfine field values of the Si-4 samples fluctuate in the range of uncertainty, i.e., between 27.3 and 27.6 T.

Table 3 Parameters of Mössbauer spectra of the nanocrystalline Fe₈₂₍₇₈₎Si₄₍₈₎B₁₀P₃Cu₁ alloys annealed at 420 °C for 20 and 60 min (*A*₂₃ and *B*_{hf} values are the average values of the respective quantities of the components representing amorphous/crystalline phase)

Alloy	Relative fraction of the component						
	A8 [%]	A8 / IF_1 [%]	A7 [%]	A6 / IF_2 [%]	AM [%]	A ₂₃ [-]	B _{hf} [T]
Fe₈₂Si₄B₁₀P₃Cu₁							
20 min, vacuum	4	18	14	12	53	3.1	27.5
60 min, vacuum	16	20	6	4	54	2.8	27.6
20 min, Ar	5	19	14	15	47	2.9	27.3
60 min, Ar	15	21	6	3	55	2.5	27.5
	A8 [%]	A7 / IF_1 [%]	A6 / IF_2 [%]	IF_3 [%]	AM [%]	A ₂₃ [-]	B _{hf} [T]
Fe₇₈Si₈B₁₀P₃Cu₁							
20 min, vacuum	4	28	13	6	49	2.9	26.7
60 min, vacuum	5	27	9	5	56	2.9	26.7
20 min, Ar	4	30	11	8	46	2.6	26.6
60 min, Ar	4	29	11	9	48	3.1	26.6

Mössbauer spectra of samples with higher silicon content (Si-8) show rounded envelope pointing at a lower abundance and/or a lower degree of ordering of the highest field A8 phase as compared to the Si-4 alloys. This tendency is also reflected by a lower fraction of the corresponding A8 (orange) component covering barely 5% of the spectra area even after 60 min of annealing. The green field-distributed component became hence more pronounced with the average *B*_{hf} of about 31.4–31.5 T and can be in this case more likely attributed to an A7 coordination surroundings as to an interface between A8/A7. The next ochre coloured component describes the hyperfine field distribution of about 27.5 T, which is slightly lower than the *B*_{hf} value reported for the A6 coordination. Due to the field distribution, we assigned this component to the A6 phase and/or interface between the A6 and the lower-field vicinities (labelled IF_2). The next blue component with lower *B*_{hf} values of about 24 T is comparable in abundance with the former and it is labelled as IF_3 assuming to represent a kind of an intermediate phase. The last (violet) broad distribution adjacent to the low-field amorphous rest covers the largest part of the spectra for all cases. Its volumetric fraction is below 50% for 20-min annealed alloys in both atmospheres. After 60-min annealing, some phase redistribution was observed (refer to Table 3), the average *B*_{hf} remained, however, unchanged.

The *A*₂₃ parameter of the partially crystallized samples (both atmospheres) increased as compared to their amorphous counterparts for both Si-4 and Si-8 alloys. For Si-4 alloy, the *A*₂₃ parameter is lower for Ar-annealed samples as compared to the samples annealed in vacuum. This behaviour can be due to the surface crystallization after annealing in Ar atmosphere increasing the density of the surface layer squeezing the magnetostrictive volume beneath [14]. This effect has been already reported for low-Si FINEMETs annealed in Ar ambience [10, 15]. Although it is expected to be much weaker in Fe-Si-B-P-Cu alloys [9], it drives the *A*₂₃ parameter out of the ribbon plane and this tendency is enhanced by prolonged annealing time resulting in advanced crystallization process (see decreasing tendency of *A*₂₃ with annealing time for Si-4 sample). In Si-8 alloys, an opposite tendency of the *A*₂₃ parameter to increase after longer annealing was observed, pointing at different mechanisms acting in this kind of alloy as compared to Si-4.

In case of very complex Mössbauer spectra consisting of many overlapping components, the fitting procedure might often dim the obtained results. Therefore, a very important step of spectra shape visual observation and comparison cannot be omitted in such cases to judge the relevancy of the resultant parameters. If we inspect visually the spectra of the alloys annealed in vacuum (left column in Fig. 3) and in argon (right column in Fig. 3), the changes visible to the naked eye are very small. The most prominent is the difference for Si-8 alloy after 20 min annealing (third row in Fig. 3) highlighted by red circles, which point at some phase redistribution and/or change of the net magnetic moment direction (A_{23} value) of the individual components (in Table 3 presented only as an average value for all components).

3.3 Magnetic measurements

Amorphous precursors of Si-4 and Si-8 alloys show hysteresis loops that have a round shape with gradual saturation as seen in Fig. 4. Sample Si-4 revealed higher saturation magnetic polarization $J_s = 1.35$ T than Si-8, where $J_s = 1.27$ T (see Table 4). Moreover, the slope of the loop is smaller for the Si-8 sample than for Si-4, which also corresponds to the lower value of the magnetization work, W . Figure 5 shows the hysteresis loops after annealing at 420 °C for 20 and 60 min in vacuum and in Ar, respectively. With the structural change from amorphous to nanocrystalline structure, J_s increased rapidly. J_s values for Si-4 material increased to 1.61 T after Ar annealing and to 1.65 T for 20 min and to 1.66 T for 60 min annealing time after vacuum annealing, respectively. The nanocrystalline Si-8 sample exhibited an increase to the values $J_s = 1.60$ T and 1.64 T for Ar and for vacuum atmosphere, respectively. The moderate increase in the value of saturation magnetic polarization is due to the higher content of crystallinity after vacuum annealing. The significant increase in resultant coercivity, H_c after nanocrystallization and with annealing time was observed for both compositions. We assume that this increase in coercivity is caused by the grain size, which grows in this type of material rapidly, especially with a longer annealing time. Therefore, some authors use the rapid annealing to achieve finer grains and to optimize soft magnetic properties [16]. The observed higher values of H_c for vacuum annealed samples could be explained by the larger grain size observed after vacuum (Si-4: ≤ 58 nm and Si-8: ≤ 81.2 nm) than after Ar annealing (Si-4: ≤ 55.9 nm and Si-8: ≤ 79.9 nm) as determined by XRD measurements. Such grain sizes usually cause magnetic hardening in Fe-based materials. In contrast, the results of AFM measurements (next below) indicate smaller grains on the surface of vacuum samples than on Ar surfaces. These results support

Fig. 4 Hysteresis loops of the as-cast $\text{Fe}_{82(78)}\text{Si}_{4(8)}\text{B}_{10}\text{P}_3\text{Cu}_1$ alloys

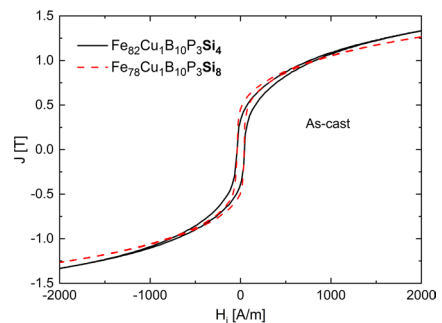


Table 4 Magnetic properties of $Fe_{82}Si_{14}B_{10}P_3Cu_1$ alloys: as-cast and annealed 20 and 60 min at 420 °C in vacuum and argon

Alloy	H_c [A/m]		J_s [T]		W [J/m ³]	
	As-cast	420 °C/ 20 min	As-cast	420 °C/ 20 min	As-cast	420 °C/ 20 min
$Fe_{82}Si_{14}B_{10}P_3Cu_1$	41	vacuum	1.35	vacuum	613	vacuum
		78.8		1.65		43
$Fe_{78}Si_{18}B_{10}P_3Cu_1$		Ar		Ar		Ar
	38	66	1.27	1.61	513	30
		vacuum		vacuum		vacuum
		62.9		1.64		32
		Ar		Ar		Ar
		42	65	1.60	1.60	13

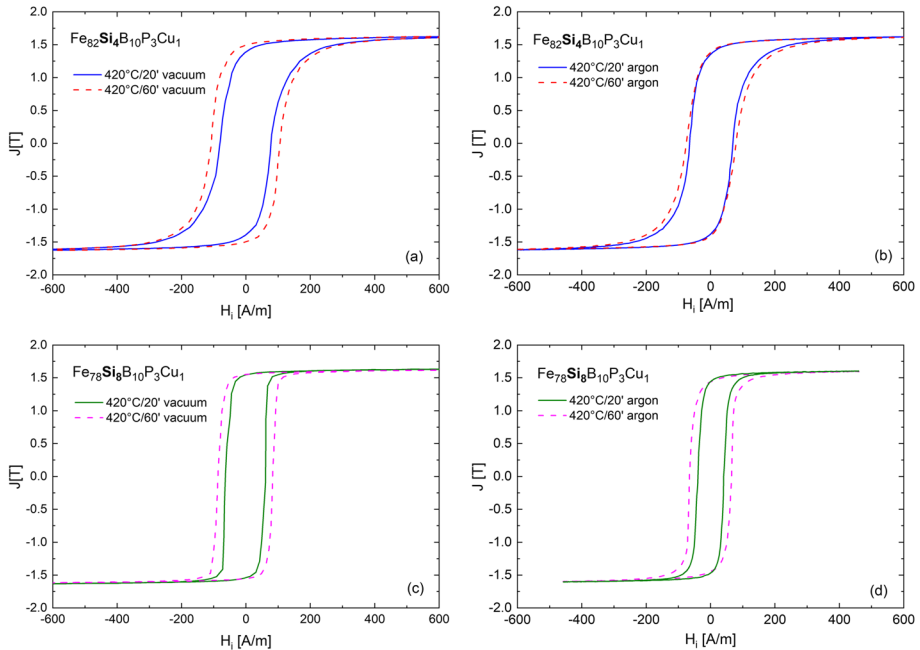


Fig. 5 Hysteresis loops of the nanocrystalline $\text{Fe}_{82}\text{Si}_4\text{B}_{10}\text{P}_3\text{Cu}_1$ (**a**, **b** – top row) and $\text{Fe}_{78}\text{Si}_8\text{B}_{10}\text{P}_3\text{Cu}_1$ (**c**, **d** – bottom row) alloys annealed for 20 and 60 min at 420 °C in vacuum (**a**, **c** – left column) and in Ar (**b**, **d** – right column)

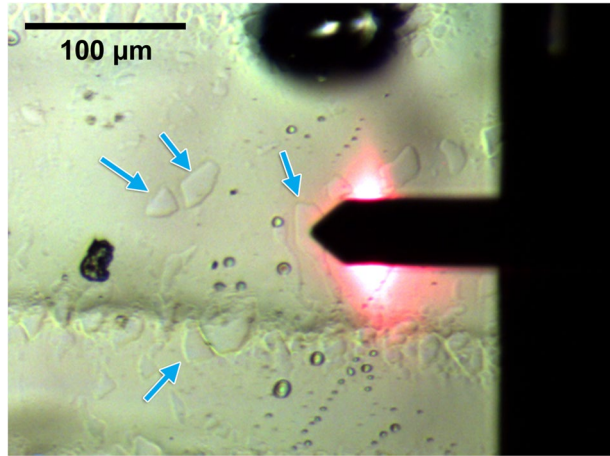
the possibility of influence of macroscopic heterogeneity and surface effect in Ar annealed samples [10, 14]. In addition, it should be mentioned that these NANOMET-type materials contain phosphorus and therefore the surface effect is not as pronounced here as it was observed in low-Si FINEMETs [14].

Better magnetic softness was shown by the Si-8 sample after 20 min-annealing, whose H_c value is the lowest as well as the determined magnetization work, W (see Table 3). A low value of magnetization work indicates the dominance of longitudinal magnetic anisotropy in the easy direction of magnetization, in this case along the tape axis.

3.4 Atomic force microscopy

As the rapidly quenched ribbons usually show large surface-to-volume ratio, the features of their surfaces have significant effect on their overall physical properties. For example, differences in the bulk and surface crystallization are well-known for metal-metalloid glasses. Surface crystallization and oxidation were also shown to be responsible for the magnetoelastic effects in the amorphous metals [17]. In the low-Si magnetostrictive alloys, the macroscopic heterogeneity established during Ar annealing was observed [18] and attributed to the so-called surface squeeze effect affecting their magnetic anisotropy [10]. Whereby, the major contribution to this squeezing stress in medium-Si FINEMETs (10 at. %) was attributed to the surface crystallization, not to surface oxidation since no contiguous oxide layer was identified [10].

Fig. 6 The shiny side of the studied as-quenched $\text{Fe}_{82}\text{Si}_4\text{B}_{10}\text{P}_3\text{Cu}_1$ ribbon



In this sense, we have applied a surface sensitive technique of atomic force microscopy (AFM) to inspect the structure of the studied alloys surfaces after annealing in various atmospheres. Surfaces of the shiny side of the ribbons (exposed to air during quenching process) were analysed. The surrounding of the scanned surfaces was also captured by the optical camera of the AFM microscope.

3.4.1 As-cast alloys

The shiny side of the Si-4 ribbon inspected under optical camera is shown in Fig. 6. The image shows high structural nonuniformity of the sample surface. Numerous polygonal formations highlighted by blue arrows in the figure are concentrated preferentially at the places where the height changes sharply. Isolated polygonal formations have a surface undisturbed by other objects within their interior. Their interior has a light, unchanging shade of colour. Therefore, it can also be expected that within polygonal formations the structure of the surface will be homogeneous.

Using the AFM microscope, we mapped the centre of the polygonal formation and also the area outside these formations with a single $50 \times 50 \mu\text{m}^2$ scan. The resulting image of the topography can be seen in Fig. 7a. The colour palette of the image is inverted to see the numerous local changes in the topography better resolved. This means that higher places on the surface correspond to a dark shade of colour and lower places to a light shade of colour. The dimensions of the polygonal structure in Fig. 7a (a large dark spot in the centre of the upper half of the image), are about $33.6 \times 18.0 \mu\text{m}$. The height of the formation is approximately 75 nm. Furthermore, large circular shaped objects (up to 5.7 μm in diameter) can be seen on the surface of the scanned area. Some of them were too tall and distracted from the polygonal formations. Therefore, the height of the entire image was limited to 100 nm.

In Fig. 7a, we can also notice that the surface is completely covered with small protrusions, which are shown in detail in Fig. 7b. The protrusions of the round plan had a height of 14.1 ± 2.9 nm outside polynomial elevations. When Fig. 7a was rendered using a different colour palette, it was seen that small protrusions were also found on the polygonal elevations. This means that they formed later than the elevations.

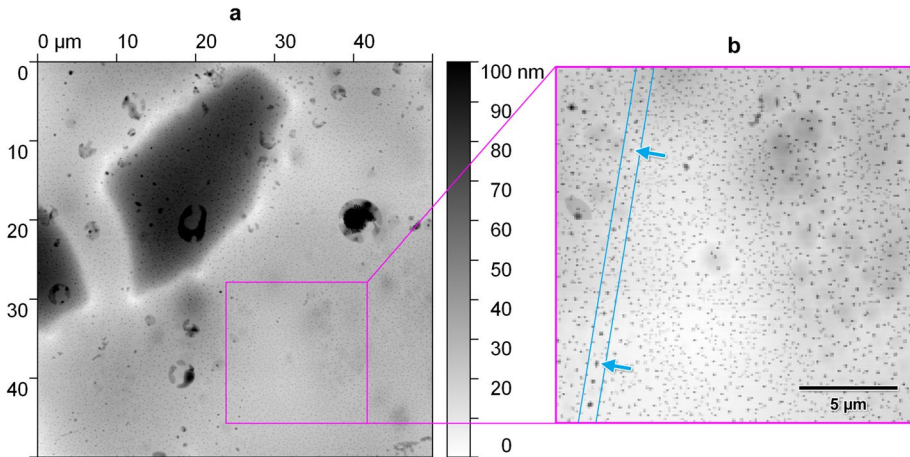


Fig. 7 **a**) AFM image of the surface topography of the as-quenched $\text{Fe}_{82}\text{Si}_4\text{B}_{10}\text{P}_3\text{Cu}_1$ alloy capturing the polygonal elevations that were seen in the optical camera (in Fig. 6); **b**) software-enlarged section of the image. Two slanted lines delineate the area where the protrusions (see arrows) are positioned in a line

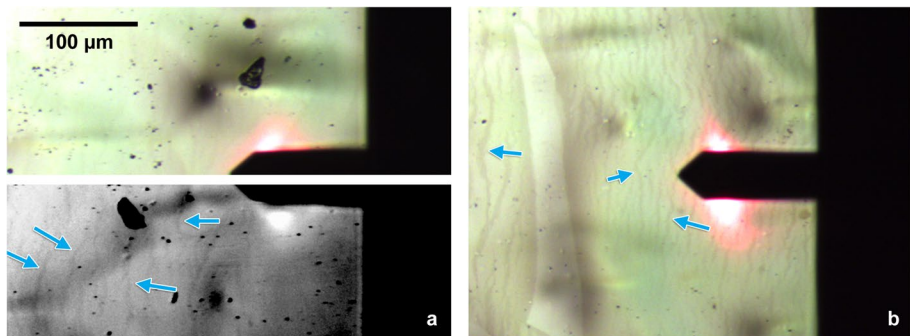
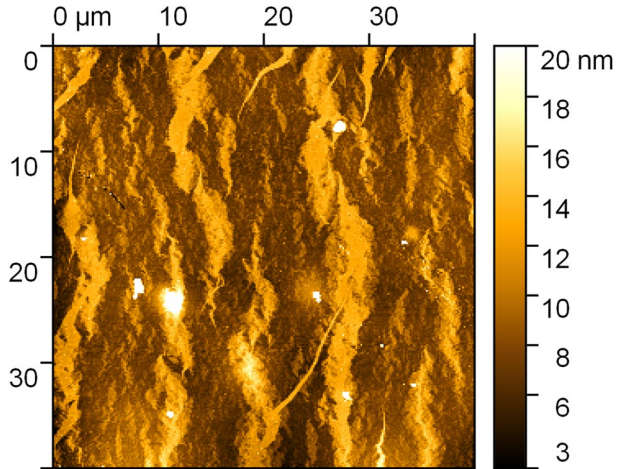


Fig. 8 **a**) The surface of the shiny side of the as-quenched $\text{Fe}_{78}\text{Si}_8\text{B}_{10}\text{P}_3\text{Cu}_1$ ribbon in the optical camera of the AFM microscope. The lower part of the photo has increased contrast, thanks to which vertical dark bands (see arrows) are visible in the image. **b**) A sample of the same composition annealed for 60 min in a vacuum at a temperature of 420 °C

At certain places of the scanned surface, these small protrusions are situated one behind the other in one line (see arrows in Fig. 7b). In the original image (Fig. 7a), the length of this line is about 28 μm . Although the regularity in the position of these protrusions is similar to oxides formation, they could be also attributed to an unusual structure typical for the low-Si melt-spun alloys showing a large amount of extremely small $\alpha\text{-Fe}$ grains inside bulk ($\sim 2 \div 3$ nm in size) referred to as a nanohetero-amorphous structure [19]. It should be noted that the AFM method does not allow elemental analysis and therefore it is not possible to identify unambiguously the observed protrusions using this technique.

The surface structure of the Si-8 alloy after production differs from the alloy with lower silicon content (Fig. 8a). In the optical camera, no polygonal elevations were visible on the inspected surfaces, though very indistinct vertical lines oriented preferentially perpendicular to the ribbon pulling direction can be seen. The lower half of Fig. 8a has artificially

Fig. 9 The area on the surface of the shiny side of the $\text{Fe}_{78}\text{Si}_8\text{B}_{10}\text{P}_3\text{Cu}_1$ ribbon imaged by the AFM microscope. The alloy was annealed for 60 min in a vacuum at a temperature of 420 °C. The exact location of the scan is captured in Fig. 8b



increased contrast to visualise better the vertical lines (see arrows) with spacing roughly 20 μm. After annealing the sample, these vertical lines are highlighted themselves in the optical camera (Fig. 8b), indicating greater differences in surface morphology between the regions lying between and along the lines.

The vertical lines can be seen much more clearly in the AFM image shown in Fig. 9. Here, the bright bands correspond to protrusions on the surface, the height of which is approximately the same, 5 nm. In addition to the vertical lines on the surface of the annealed Si-8 sample, polygonal elevations are also visible, which were not visible on the surface of the as-cast sample.

The orientation of the vertical lines on the Si-8 ribbon surface can probably be related to the periodic surface defects that sometimes occur in planar flow casting when a puddle of molten metal vibrates in the space between the nozzles and the cylinder [20]. Although the period of these defects is usually at the level of millimetre units, they change the character of the surface of the entire ribbon. Therefore, theoretically, vertical lines can have an orientation imposed by the conditions of ribbon production.

3.4.2 Annealed alloys

When scanning the surfaces of the annealed samples with the AFM microscope, we focused only on the centres of the areas of polygonal elevations. That is because the measurements in these areas were reproducible regardless of which polygonal elevation was scanned. The average height of grain-like protrusions measured on both as-cast and annealed samples is summarized in Table 5 (up to 30 protrusions heights were averaged). The table shows the average height of the protrusions, as this parameter is more accurate than the width of the protrusions in AFM microscopy.

Based on Table 5 we can conclude that the height of the protrusions on the polygonal elevations changed for neither of the alloy compositions after vacuum annealing. What has changed, however, is the density of protrusions on the surface. This increased significantly in the annealed samples (not presented here).

Samples annealed in argon had significantly higher protrusions on the shiny surface than samples annealed in vacuum (Table 5). On their surfaces it was possible to distinguish

Table 5 Height of protrusions on the surface (the shiny side) of the as-cast and annealed ribbons (annealing at 420 °C in vacuum and argon ambiances). The data after the \pm sign is the standard deviation of the arithmetic mean of the height of individual protrusions

Alloy	Height of grains / agglomerates [nm]	As-cast	
		420 °C/ 20 min	420 °C/ 60 min
$\text{Fe}_{82}\text{Si}_4\text{B}_{10}\text{P}_3\text{Cu}_1$	6.9 ± 2.6	vacuum	
			5.2 ± 1.1
		Ar	2.6 ± 0.5
$\text{Fe}_{78}\text{Si}_8\text{B}_{10}\text{P}_3\text{Cu}_1$	5.6 ± 1.4		$30 \pm 6 / 49 \pm 10$
		vacuum	$28 \pm 5 / 58 \pm 8$
		Ar	
$\text{Fe}_{82}\text{Si}_4\text{B}_{10}\text{P}_3\text{Cu}_1$	6.2 ± 2.1		4.4 ± 1.9
		vacuum	
		Ar	
$\text{Fe}_{78}\text{Si}_8\text{B}_{10}\text{P}_3\text{Cu}_1$	$29 \pm 4 / 71 \pm 6$		$46 \pm 11 / 110 \pm 17$
		vacuum	
		Ar	

two types of protrusions clearly. The lower protrusions resembling grains and the higher belonging to agglomerates of grains. Some agglomeration was also observed on the surfaces of the as-cast ribbons of both compositions, but due to the small size of the grains it was difficult to distinguish between incipient agglomerates and individual grains. Therefore, the average height of all protrusions is given in Table 5 for the as-cast samples. After argon annealing, the height of the individual grains on the surface of the Si-4 samples did not change with increasing annealing time, however, the number of grain agglomerates per unit area has increased. In the Si-8 sample, the grains and agglomerates continued to grow after 20 min of annealing. In addition to the protrusions of the average height of which listed in Table 5, several micrometre-high protrusions (resembling oxides) were visible on the surfaces of the samples annealed in argon atmosphere. Due to their large size, the AFM method is not suitable for their analysis.

Additional description of the results of AFM measurements of alloys annealed in argon, together with images of their surfaces, can be found in our previous publication [21].

By comparing the samples annealed in vacuum and argon at 420 °C, we can come to the clear conclusion that annealing in argon leads to a more significant grain growth on the shiny surface of the ribbons. Annealing the alloys in vacuum increased the density of protrusions on the surface, however, their average height did not change.

4 Conclusions

The effect of annealing ambience and duration on the structural and magnetic properties of $\text{Fe}_{82}\text{Si}_4\text{B}_{10}\text{P}_3\text{Cu}_1$ and $\text{Fe}_{78}\text{Si}_8\text{B}_{10}\text{P}_3\text{Cu}_1$ alloys was studied by a combination of different analytical techniques. According to the obtained results, the following conclusions can be made:

1. Different silicon content of 4 at. % and 8 at. % (at the expense of Fe) in NANOMETs results in formation of diverse structures after their production. XRD disclosed a relatively high content of a crystalline phase present in $\text{Fe}_{82}\text{Si}_4\text{B}_{10}\text{P}_3\text{Cu}_1$ as-cast alloy (assumingly the so-called nanohetero-amorphous structure), though, the $\text{Fe}_{78}\text{Si}_8\text{B}_{10}\text{P}_3\text{Cu}_1$ alloy proved to be fully amorphous inside the bulk. This structural diversity obviously played a significant role in different behaviour of the alloys observed under various annealing conditions.

2. The annealing ambience has pronounced effect on the structure of alloy surfaces confirmed by AFM measurements. AFM identified lower protrusion heights on the surfaces of the alloys annealed in vacuum as compared to argon, where also larger formations (agglomerates) were observed. This might indicate the influence of the above-mentioned macroscopic heterogeneity and surface effect in samples annealed in argon. Although the presence of oxides on the sample surfaces was excluded by GIXRD, the more sensitive technique of Energy Dispersive Spectroscopy (EDS) will be applied in further to quantify the elemental compositions of sample surfaces and thus to verify the presence of oxides on the surfaces.
3. Due to small physical dimensions of the ribbons, their surfaces affect the bulk structural characteristics and the resultant measurable physical properties. Mössbauer spectroscopy indicated gentle changes in structural arrangement of the identified iron surroundings and gave a hint on the reorientation of the net magnetic moments. Though, the microstructural changes manifested macroscopically to a larger extent in magnetic measurements as decreased coercivity and magnetization work after argon annealing for both studied compositions. These observations agree with the observed decreasing tendency of the grain size in the bulk determined by XRD technique in argon annealed alloys.
4. Longer annealing times tend to increase the bulk grain size and consequently led to a higher coercivity in both annealing ambiances for both $\text{Fe}_{82}\text{Si}_4\text{B}_{10}\text{P}_3\text{Cu}_1$ and $\text{Fe}_{78}\text{Si}_8\text{B}_{10}\text{P}_3\text{Cu}_1$ alloys.

Author contribution All authors contributed to the study conception and design. All authors read and approved the final manuscript.

Conceptualization: Katarína Sedlačková, Jozef Sitek; Formal analysis and investigation: Katarína Sedlačková, Beata Butvinová, Milan Pavúk, Július Dekan and Patrik Novák; Material preparation: Beata Butvinová, Stanislav Sojak. Writing—original draft preparation: Katarína Sedlačková, Beata Butvinová, Milan Pavúk; Writing—review and editing: all authors; Supervision: Jozef Sitek.

Funding This work was partially supported by grants of the Slovak Research and Development Agency No. APVV-19-0369 and of the Scientific Grant Agency of the Ministry of Education, Science, Research and Sport of the Slovak Republic No. 1/0130/20 and No. 2/0144/21.

Availability of data and materials Not applicable.

Declarations

Ethical approval Not applicable.

Competing interests The authors have no competing interests as defined by Springer, or other interests that might be perceived to influence the results and/or discussion reported in this paper.

References

1. Lashgari, H.R., Chu, D., Xie, S., Sun, H., Ferry, M., Li, S.: Composition dependence of the microstructure and soft magnetic properties of Fe-based amorphous / nanocrystalline alloys : A review study. *J. Non. Cryst. Solids*. **391**, 61–82 (2014). <https://doi.org/10.1016/j.jnoncrysol.2014.03.010>
2. McHenry, M.E., Johnson, F., Okumura, H., Ohkubo, T., Ramanan, V.R.V., Laughlin, D.E.: The kinetics of nanocrystallization and microstructural observations in FINEMET, NANOPERM and HITPERM nanocomposite magnetic materials. *Scr. Mater.* **48**, 881–887 (2003). [https://doi.org/10.1016/S1359-6462\(02\)00597-3](https://doi.org/10.1016/S1359-6462(02)00597-3)

3. Nishiyama, N., Tanimoto, K., Makino, A.: Outstanding efficiency in energy conversion for electric motors constructed by nanocrystalline soft magnetic alloy “ NANOMET ® ” cores Outstanding efficiency in energy conversion for electric motors constructed by nanocrystalline soft magnetic. *AIP Adv.* 055925, (2016). <https://doi.org/10.1063/1.4944341>
4. Makino, A., Men, H., Kubota, T., Yubuta, K., Inoue, A.: FeSiBPCu nanocrystalline soft magnetic alloys with high B s of 1.9 Tesla produced by crystallizing hetero-amorphous phase. *Mater. Trans.* **50**, 204–209 (2009). <https://doi.org/10.2320/matertrans.MER2008306>
5. Makino, A.: Nanocrystalline soft magnetic Fe-Si-B-P-Cu alloys with high B of 1.8–1.9T contributable to energy saving. *IEEE Trans. Magn.* **48**, 1331–1335 (2012). <https://doi.org/10.1109/TMAG.2011.2175210>
6. Meng, Y., Pang, S., Chang, C., Wang, G.: Magnetic softening of the Fe83 Si3B11P2Cu1 amorphous / nanocrystalline alloys with large-size pre-existing a -Fe grains by high heating-rate annealing. *J. Mater. Res. Technol.* **20**, 161–168 (2022). <https://doi.org/10.1016/j.jmrt.2022.07.051>
7. Parsons, R., Garitaonandia, J.S., Yanai, T., Onodera, K., Kishimoto, H., Kato, A.: Effect of Si on the field-induced anisotropy in Fe-rich nanocrystalline soft magnetic alloys. *J. Alloys Compd.* **695**, 3156–3162 (2017). <https://doi.org/10.1016/j.jallcom.2016.11.330>
8. Butvinová, B., Vlasák, G., Butvin, P., Ileková, E.: Magnetic properties and dilatation of FeNbCuBSi alloys. *Acta Phys. Slovaca.* **51**, 1–7 (2001)
9. Butvinová, B., Butvin, P., Maňko, I., Janičkovič, D., Kuzminski, M.: Accents in modern high saturation nanocrystalline Fe-Rich alloys. *ACTA Phys. Pol. A.* **131**, 711–713 (2017). <https://doi.org/10.12693/APhys PolA.131.711>
10. Butvinová, B., Butvin, P., Maňko, I., Kadlečková, M., Kuzminski, M., Švec, P., Jr.: Surface mediated impact of thermal treatment ambience on magnetic properties of Fe–Nb–Cu–B–Si nanocrystalline ribbons. *Appl. Surf. Sci.* **301**, 119–125 (2014). <https://doi.org/10.1016/j.apsusc.2014.01.199>
11. Žák, T., Jirásková, J.: CONFIT: Mossbauer spectra fitting program. *Surf. Interface Anal.* **38**, 710–714 (2006). <https://doi.org/10.1002/sia.2285>
12. Cao, C.C., Wang, Y.G., Zhu, L., Meng, Y., Zhai, X.B., Dai, Y.D., Chen, J.K., Pan, F.M.: Local structure, nucleation sites and crystallization behavior and their effects on magnetic properties of Fe₈₁Si_xB₁₀P_{8-x}Cu₁ (x = 0–8). *Sci. Rep.* 1–11 (2018). <https://doi.org/10.1038/s41598-018-19665-8>
13. Stearns, M.B.: Internal magnetic fields, isomer shifts, and relative abundances of the various Fe sites in FeSi alloys. *Phys. Rev.* **129**, (1963)
14. Butvin, P., Šitek, J., Butvinová, B., Ileková, E.: Unusual magnetic anisotropy of Si-poor FeNbCuBSi. *J. Phys. IV Fr.* **8**, 123–126 (1998)
15. Butvinová, B., Butvin, P., Brzózka, K., Kuzminski, M., Maňko, I., Švec, P., Sr., Chromčíková, M.: Effects of surface crystallization and oxidation in nanocrystalline FeNbCuSiB(P) ribbons. *J. Magn. Magn. Mater.* **424**, 233–237 (2017). <https://doi.org/10.1016/j.jmmm.2016.10.068>
16. Zhang, B., Yang, F., He, A., Xiao, H., Dong, Y., Li, J., Han, Y.: Rapid annealing optimizing magnetic softness and thermal stability of Mn-substituted Fe-based nanocrystalline alloys. *Metals (Basel)*. **11**, (2021). <https://doi.org/10.3390/met111010020>
17. Životský, O., Postava, K., Kraus, L., Jirásková, Y., Juraszek, J., Teillet, J., Barčová, K., Švec, P., Janičkovič, D., Pištora, J.: Surface and bulk magnetic properties of as-quenched FeNbB ribbons. *J. Magn. Magn. Mater.* **320**, 1535–1540 (2008). <https://doi.org/10.1016/j.jmmm.2008.01.003>
18. Butvinová, B., Butvin, P., Schäfer, R.: Influence of heterogeneity on magnetic response of nanocrystalline ribbons. *Sensors Actuators A.* **106**, 52–55 (2003). [https://doi.org/10.1016/S0924-4247\(03\)00132-8](https://doi.org/10.1016/S0924-4247(03)00132-8)
19. Makino, A., Men, H., Kubota, T., Yubuta, K., Inoue, A.: New excellent soft magnetic FeSiBPCu nanocrystallized alloys with high Bs of 1.9 T from nanohetero-amorphous phase. *IEEE Trans. Magn.* **45**, 4302–4305 (2009). <https://doi.org/10.1109/TMAG.2009.20238623>
20. Byrne, C.J., Theisen, E.A., Reed, B.L., Steen, P.H.: Capillary puddle vibrations linked to casting-defect formation in Planar-Flow melt spinning. *Metal. Mater. Trans. B.* **37**, 445–456 (2006)
21. Šitek, J., Sedláčková, K., Butvinová, B., Dekan, J., Pavúk, M.: Structural and Magnetic Properties of Nanocrystalline FeSiBPCu Alloy. *AIP Conf. Proceedings, Appl. Phys. Condens. Matter APCOM 2022, Štrbské Pleso, Slovak Republic*, in press

Publisher's note Springer Nature remains neutral with regard to jurisdictional claims in published maps and institutional affiliations.

Springer Nature or its licensor (e.g. a society or other partner) holds exclusive rights to this article under a publishing agreement with the author(s) or other rightsholder(s); author self-archiving of the accepted manuscript version of this article is solely governed by the terms of such publishing agreement and applicable law.